Supporting information for

Sandwich hydrogel with confined plasmonic Cu/carbon cells for efficient solar water purification

Cheng Tian,[#a] Chengcheng Li,[#a] Delun Chen,[#a] Yifan Li,[a] Lei Xing,[b] Xinlong Tian,[a] Yang Cao,[a] Wei Huang,[*a] Zhongxin Liu,[*a] and Yijun Shen[*a]

[a] *State Key Laboratory of Marine Resource Utilization in South China Sea, Hainan University, Haikou 570228, P. R. China.*

[b] *Department of Engineering Science, University of Oxford, OX1 3PJ, UK.*

[#] Cheng Tian, Chengcheng Li, and Delun Chen contributed equally to this work.
[*] Corresponding authors: huangwei@hainanu.edu.cn, liuzhongxin@hainanu.edu.cn, yshen2000@163.com.

Note S1. The growth of Cu nanoparticles.

Cu nanoparticles are decorated on the Cu-PC through an *in situ* catalytic growth method based on the following reactions:

$$3CuCl_2 + C + 2H_2O \rightarrow Cu + 2CuCl + CO_2 + 4HCl \quad (1)$$

$$4CuCl + C + 2H_2O \rightarrow 4Cu + CO_2 + 4HCl \quad (2)$$

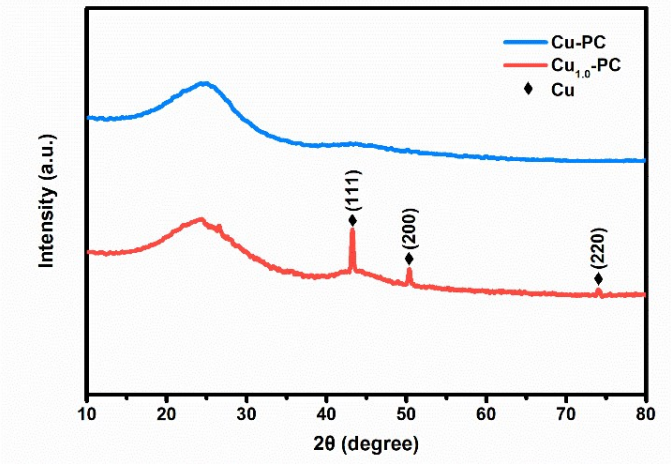

Figure S1. XRD patterns of Cu-PC and $Cu_{1.0}$-PC.

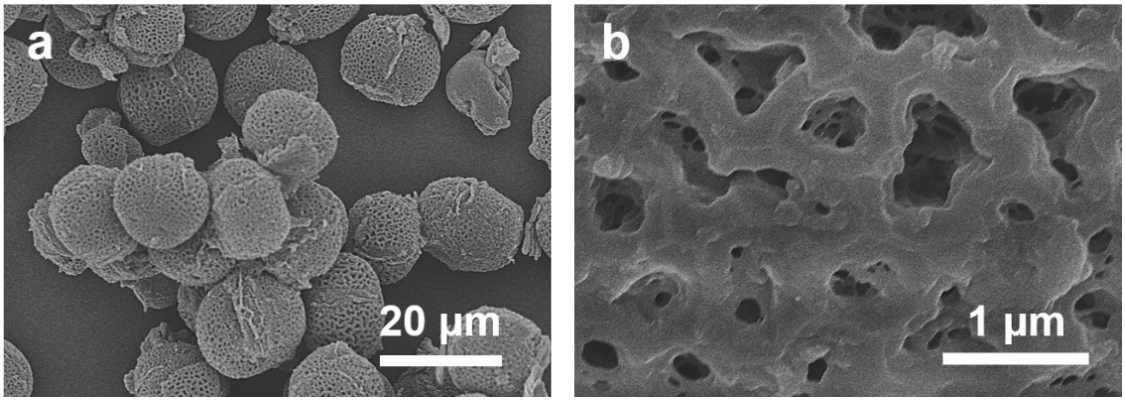

Figure S2. (a, b) The SEM images of Cu-PC.

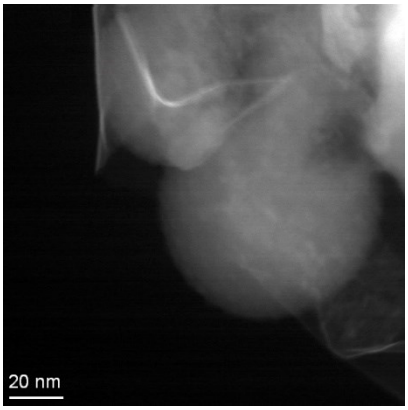

Figure S3. High-angle annular dark field (HAADF) image of the Cu particles loaded on the carbon skeleton of $Cu_{1.0}$-PC.

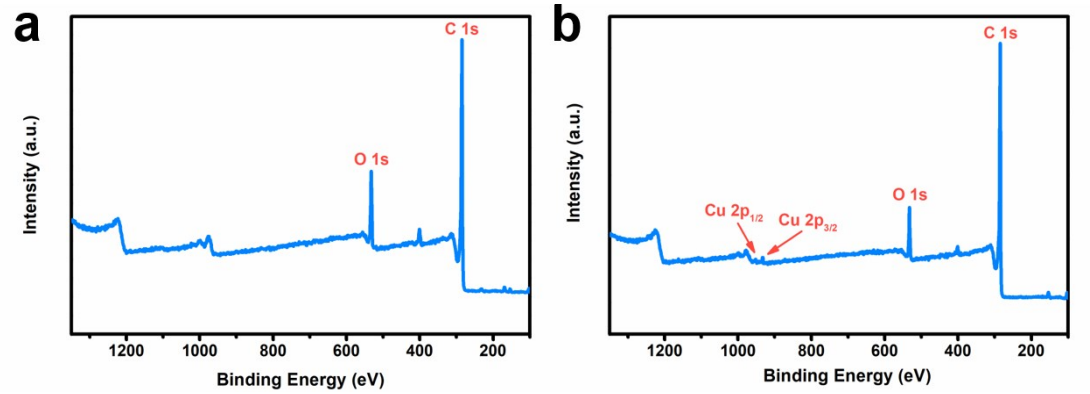

Figure S4. The XPS spectra of (a) Cu-PC and (b) $Cu_{1.0}$-PC.

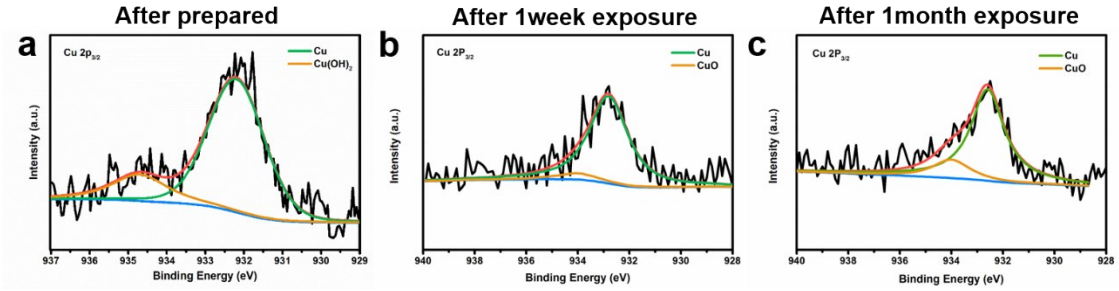

Figure S5 XPS spectra of the Cu 2p3/2 photoelectron core level for the $Cu_{1.0}$-PC: (a) as prepared soon; (b) after 1-week air exposure; (c) after 1-month air exposure.

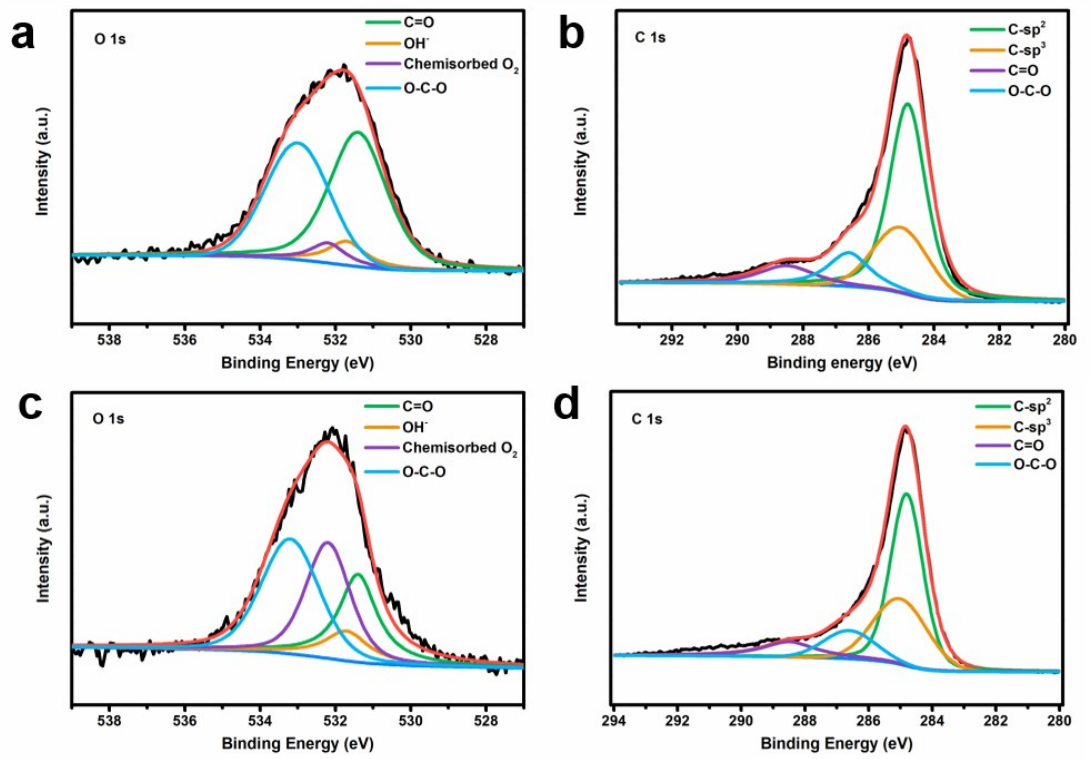

Figure S6. XPS spectra of the O 1s photoelectron core levels for (a) Cu-PC and (c) $Cu_{1.0}$-PC, and XPS spectra of the C 1s photoelectron core levels for (b) Cu-PC and (d) $Cu_{1.0}$-PC.

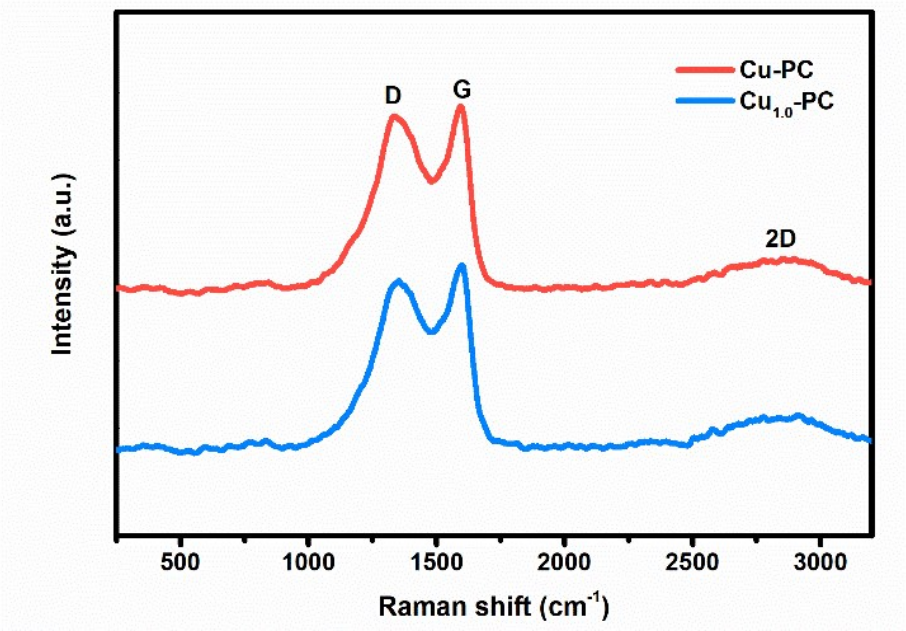

Figure S7. The Raman spectra of Cu-PC and $Cu_{1.0}$-PC.

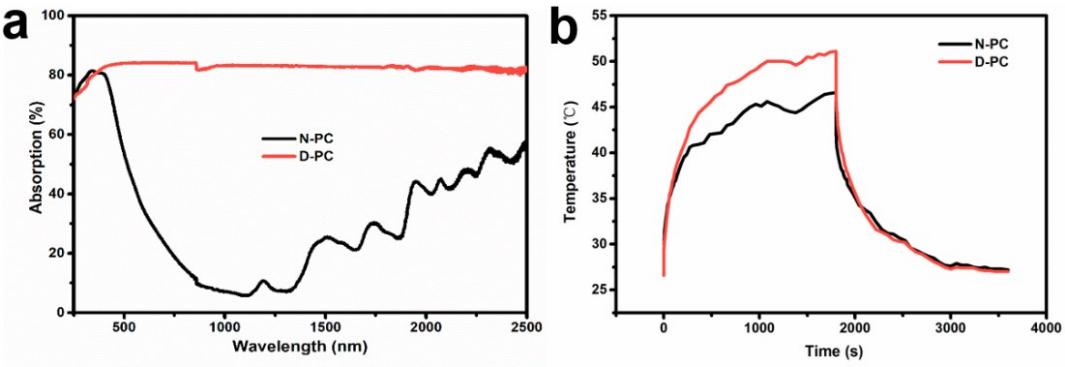

Figure S8. (a) UV-vis-NIR absorption spectrum (b) the surface temperature of N-PC (natural rape pollens) and D-PC (prepared by direct carbonize natural rape pollens without adding $CuCl_2$).

Note S2. Measurement and calculation of light-to-heat conversion efficiency.

To evaluate the light-to-heat conversion efficiency of the samples, a homemade liquid-based light absorption and heat measurement setup was established (**Figure 3a**). Briefly, 1 mL of 10 wt% PVA solution dispersed with Cu-PC or $Cu_{1.0}$-PC was added to the cuvette. Cuvette was selected as sample cell because of its high light transmission, which greatly reduces the absorption and reflection of light caused by the container. A single wavelength laser beam (i.e., 808 nm in this study) with power density of 1 W and spot size of 4×3 mm is shone right in the center of the cuvette. Partially laser light is absorbed by the dispersed solar absorbers and being converted into heat, which consequently rises the temperature of the suspensions. An IR camera was applied to record the real-time temperature change of the suspensions. As shown in **Figure 3b**, there is a sharp temperature rise as the laser turns on (about 500 s), indicating an instantaneous heat convection within the suspensions. After arriving the equilibrium temperature with fluctuation less than 0.2 °C, the laser was turned off and started the cooling process. It can be seen in **Figure S9** that the $Cu_{1.0}$-PC and the Cu-PC suspensions shows an equilibrium temperature of 43.8 °C and 40.0 °C, respectively, after 500 s of laser illumination. During the heating process, part of the light energy was absorbed and converted into heat energy by Cu-PC or $Cu_{1.0}$-PC with a light-to-heat conversion efficiency (η), which is to be investigated in this experiment. Some of the gained heat energy is converted to the internal energy of the suspensions system, indicated by a temperature increase of the suspensions before an equilibrium state is achieved. Other heat energy gets dissipated to the environment once the temperature of the suspensions is higher than the environment. Therefore, the general governing energy balance of this system is described as equation 3:

$$P\eta = \frac{dQ_i}{dt} = mC_p\frac{dT}{dt} + \frac{dQ_{ext}}{dt} \tag{3}$$

where P is the light power that is adsorbed by the suspensions and Q_i is the heat energy gained by the suspensions from the absorbed light energy, and η is the light-to-heat conversion efficiency of the sample. m, C_p, and T are mass, heat capacity, and

temperature of the suspensions, respectively. Q_{ext} is the heat dissipated into the environment external to the cuvette. The absorbed light power P is evaluated from the difference between power of the incident laser beam (P_{in}, constant at 1 W) and the outgoing light (P_{out}), which is calculated by using $Cu_{1.0}$-PC light absorbance (A_{λ}) (equation 4).

$$P = P_{in} - P_{out} \tag{4}$$

In this work, the outgoing laser intensity behind the suspensions was also monitored by a photometer. When the laser beam is turn off, energy input becomes zero and the temperature of the suspensions instantaneously starts to decline due to the heat dissipation from the suspensions to its surrounding. In this cooling stage, the energy balance equation is described by equation 5.

$$mC_p\frac{dT}{dt} + \frac{dQ_{ext}}{dt} = 0 \tag{5}$$

Generally, the heat dissipation Q_{ext} of an object to its surrounding is proportional to the temperature difference between them, and therefore it can be expressed as the following:

$$\frac{dQ_{ext}}{dt} = F(T - T_0) \tag{6}$$

where F is the proportional coefficient that describes heat loss process, T and T_0 are the temperature of the suspensions and its surrounding, in this case, ambient air. Assuming T_{eq} is the maximum suspensions temperature achieved when the equilibrium state is reached during the test, which is also the starting suspensions temperature at the time when the laser is shut, we can deduce the expression for the temperature of the suspensions (T) in this cooling stage from equation 6 and 7 as follows (equation 7):

$$T = T_0 + (T_{eq} - T_0)exp(-\frac{F}{mC_p}t) \tag{7}$$

The equation 7 can be further reorganized into equation 6, by which the F value can be

calculated from the data collected in the cooling stage, namely the stage when the laser light irradiation is off (**Figure 3b**).

$$F = -\frac{ln\frac{T_t - T_0}{T_{eq} - T_0}}{t} mC_p \tag{8}$$

Figure 3c presents $ln\frac{T - T_0}{T_{eq} - T_0}$ as a function of time (t) for Cu-PC and $Cu_{1.0}$-PC suspensions. A clearly linear correlation implies the F and mC_p can be regarded as constant in the small temperature range (25−45 °C) in our experiments. The calculated F values are listed in **Table S1**. At the equilibrium, the heat energy gained by the suspensions is equal to energy output from the suspensions by heat energy dissipation, and thus the temperature of the suspensions remains constant. In this case, the energy balance equation can be described as

$$P\eta = \frac{dQ_i}{dt} = \frac{dQ_{ext}}{dt} \tag{9}$$

Combining equation 9 with equation 4 and 6 leads to equation 8 which can be further reorganized into equation 11 for the calculation of light to heat conversion efficiency η, which is the ultimate goal of the calculations.

$$(P_{in} - P_{out})\eta = F(T_eq - T_0) \tag{10}$$

$$\eta = \frac{F(T_{eq} - T_o)}{P_{in} - P_{out}} \tag{11}$$

Thus, as one can see, in this method, the temperature profile of the suspensions in the cooling stage is used to derive the F value, which is constant across all temperatures from 25 to 45 °C and is in turn used at the equilibrium stage in calculating η. By following the procedure described above, light-to-heat conversion efficiency (η) were calculated for all tested concentrations and the calculated η in this work are listed in **Table S1**.

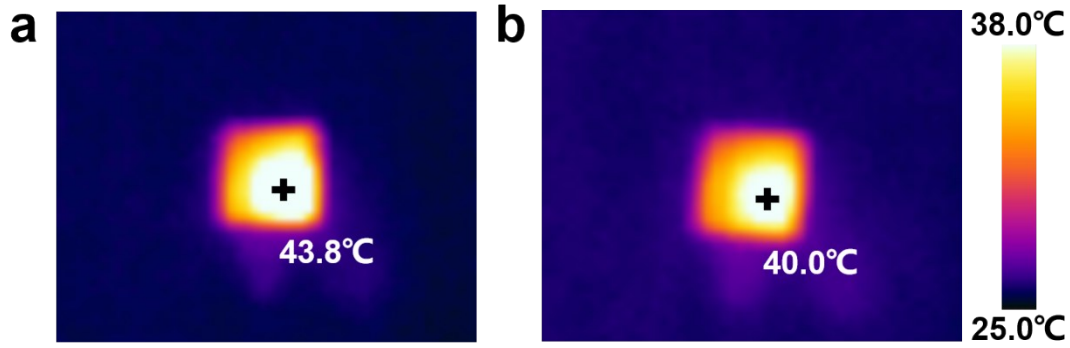

Figure S9. IR photos of the (a) $Cu_{1.0}$-PC and (b) Cu-PC suspension after 500 s of laser illumination.

Table S1. Calculated light-to-heat conversion efficiency.

808 nm wavelength laser

Sample	T_{eq}	**Time to achieve** T_{eq} **(s)**	**F (×10^{-3}/s ℃)**	η
$Cu_{1.0}$-PC	40.0	100 s	39.06	93.43%
Cu-PC	43.8	105 s	42.42	86.83%

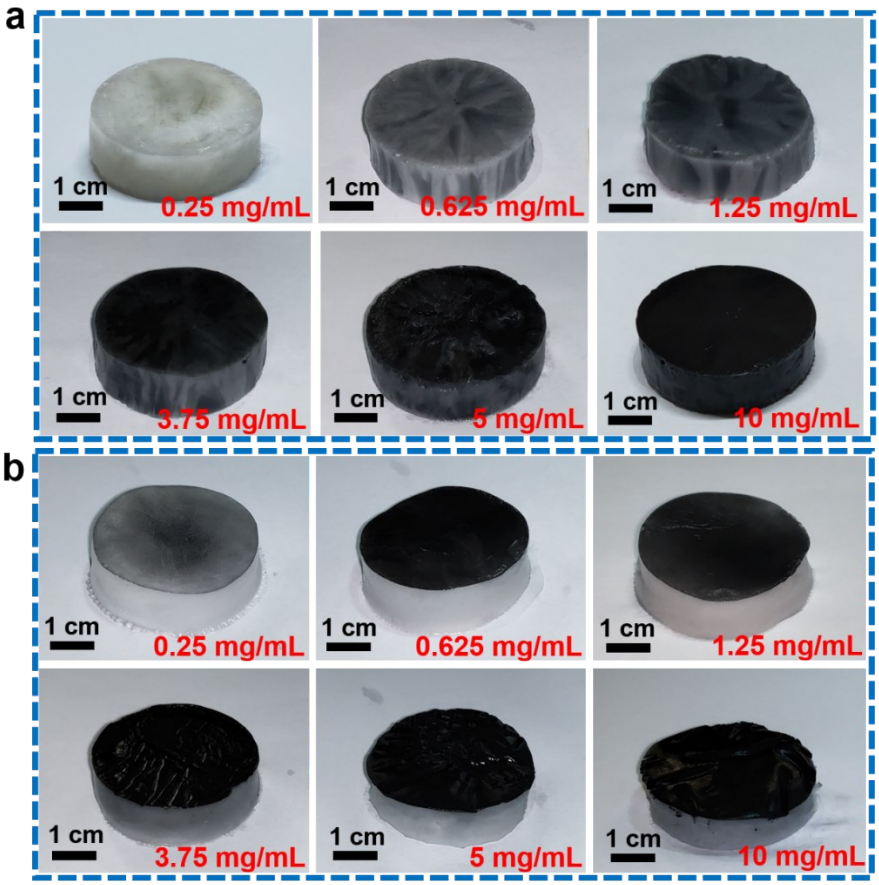

Figure S10. Optical pictures of (a) H-$Cu_{1.0}$-PC hydrogels and (b) L-$Cu_{1.0}$-PC hydrogels with different loading amounts of light absorbing materials.

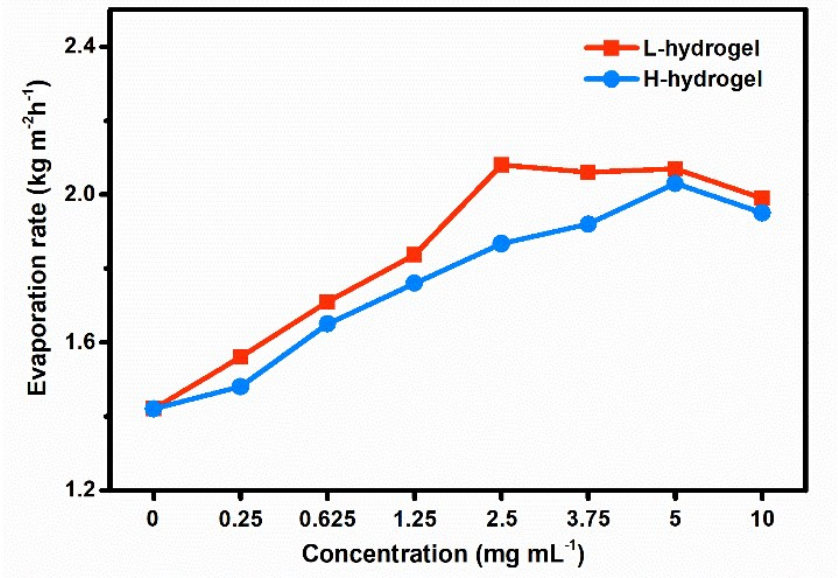

Figure S11. Water evaporation rates of hydrogels with different light absorber loadings.

Note S3. Measurement of equivalent evaporation enthalpy.

The evaporation rates were recorded to estimate the evaporation enthalpy of PVA hydrogels by making a comparison with the known theoretical value of liquid water, 2450 J/g, using identical power input (U_{in}).

$$U_{in} = \Delta H_{equ} m_g = \Delta H_o m_o \tag{12}$$

where ΔH_o and m_o refers to evaporation enthalpy and mass change of water (without hydrogel evaporator) under the dark condition, respectively. m_g is the mass change of PVA hydrogels within the same environmental condition. The obtained values of equivalent evaporation enthalpy of water in PVA hydrogels were reduced a lot compared to that of the pure water (**Figure S12)**. The energy conversion efficiency of solar steam generation is calculated as follow:

$$\eta = \frac{\dot{m} h_{LV}}{C_{opt} q} \tag{13}$$

where η is evaporation efficiency, $\dot{m}$ is the evaporation rate, h is the total enthalpy of water, C_{opt} is the optical concentration, and q is the nominal solar irradiation ($q = 1\ kW\ m^{-2}$). The value of $\dot{m}$ is obtained by subtracting the water evaporation rate without xenon lamp illumination from the water evaporation rate under 1 sun. The equivalent evaporation enthalpy estimated here was used to calculated energy efficiency in **Figure 5b**.

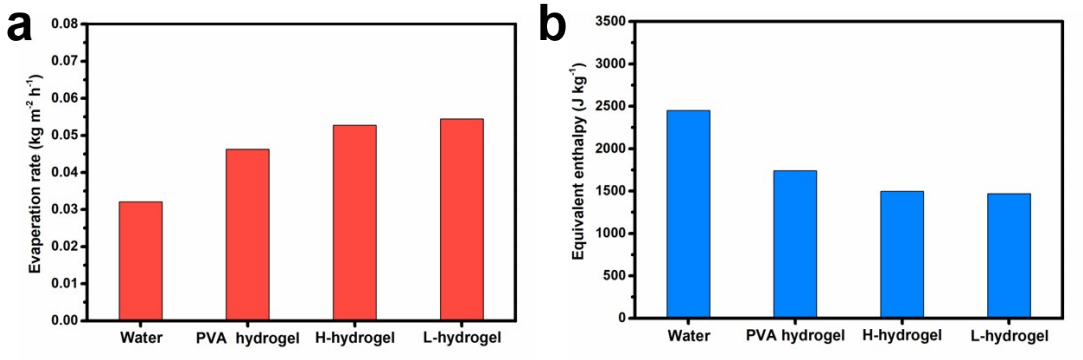

Figure S12. (a) Water evaporation rate without light irradiation and (b) equivalent enthalpy of water and hydrogels.

Note S4. Energy balance analysis.

In order to further study the energy conversion in the water evaporation process, we calculated the energy loss by the following method: the energy conversion in the whole water evaporation process is in accordance with the law of conservation of energy, so the energy conversion efficiency of the device is carefully analyzed by the following formula:

$$\dot{m}h_{LV} \cdot A_0 = C_{opt}q \cdot A_0 - \varepsilon A_0\sigma(T_1^4 - T_0^4) - hA_0(T_1 - T_2) - Cm\Delta T/t \quad (14)$$

(1) Light absorbing loss

Light absorbing process defines the total heat energy input of the system. According to the UV-Vis spectrum of different film devices, the light absorption loss is calculated by the following formula: $\psi = 1 - A$ (A is the light absorption of the device).

(2) Radiation heat loss

The radiation loss was calculated using the Stefan-Boltzmann equation:

$$\Phi = \varepsilon A_0\sigma(T_1^4 - T_0^4) \quad (15)$$

where Φ represents heat flux, ε is the emissivity, according to Kirchhoff law, the radiance and absorption of the gray body are numerically equal, so ε is defined as A, A_0 is the surface area of the device, σ is the Stefan- Boltzmann constant (5.67×10^{-8} W m^{-2} K^{-4}), T_1 is the average temperature of the device surface at a steady state condition, and T_0 is the ambient temperature (~25 ℃) upward the absorber.

(3) Convection heat loss

For convection heat loss is calculated by Newton' law of cooling as follows:

$$Q = hA_0(T_1 - T_2) \quad (16)$$

Where Q represents heat energy, h is the convection heat transfer coefficient and A_0 is the surface area of the device, T_1 is the average temperature of the device surface at a steady state condition and T_2 is the temperature of the air above the device.

The convective heat loss model of the device is natural convection of air, so heat transfer coefficient h is calculated as follows:

$$N_u = C(G_r \cdot P_r)^n \quad (17)$$

$$N_u = \frac{hl}{k} \tag{18}$$

$$h = \frac{k \cdot C(G_r \cdot P_r)^n}{l} \tag{19}$$

$$P_r = \frac{C_p \cdot \mu}{k} \tag{20}$$

$$G_r = \frac{\beta g \Delta T l^3 \rho^2}{\mu^2} \tag{21}$$

Where N_u, P_r and G_r is the Nusselt number, Prandtl number and Grashof number respectively, k is static air thermal conductivity, C and n are coefficients, β is volume expansion coefficient of air, g is gravity constant, ρ is the density of air, μ represents the dynamic viscosity of air, l is the characteristic size of material, ΔT represents the temperature differences between the film surface and the air above. However, during the evaporation process, the water vapor generates and then flows from the edge to accumulate at the center of the film surface rises into the sky, which will directly heat up the air above the material and hinder the cold air from getting close to the film surface to get heated. As a consequence, we define ΔT as the difference between the average temperature of the device surface and the average air temperature at above it.

(4) Conduction heat loss

Conduction heat loss is estimated by figuring out the sensible heat of bulk water:

$$Q = Cm\Delta T/t \tag{22}$$

Where Q is the heat energy absorbed by water, C is the specific heat capacity of water ($4.2 \times 10^3 \, J \, K^{-1} \, kg^{-1}$), m (60 g) is the weight of pure water used in this experiment, ΔT is the temperature difference of pure water after and before solar illumination under 1 sun after 1 h and t is light time (3600 s). In our experiment, the average temperature of the water below the device before and after heating is recorded by the infrared thermal imager.

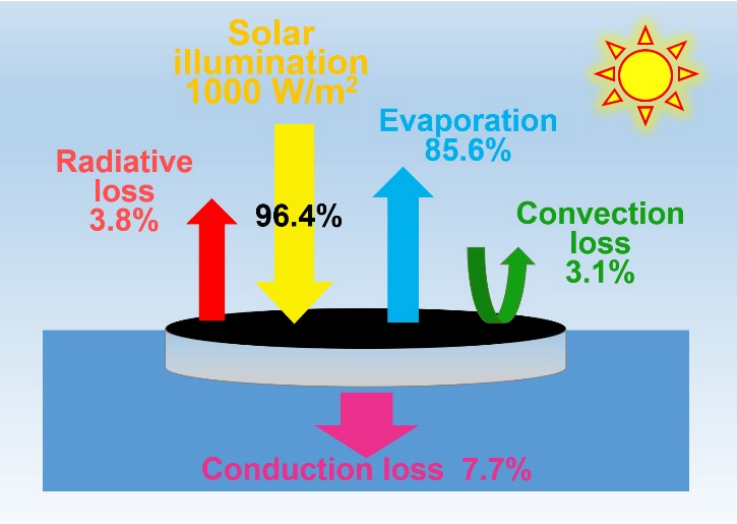

Figure S13. Energy balance and heat loss diagram of the $L_{2.5}$-$Cu_{1.0}$-PC.

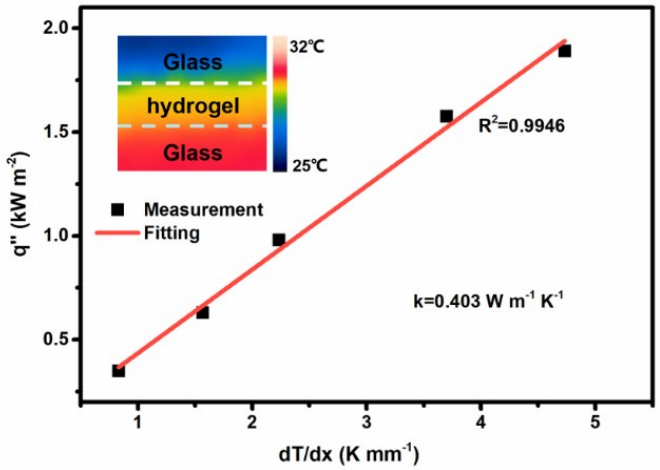

Figure S14. Thermal conductivity of the $L_{2.5}$-$Cu_{1.0}$-PC device.

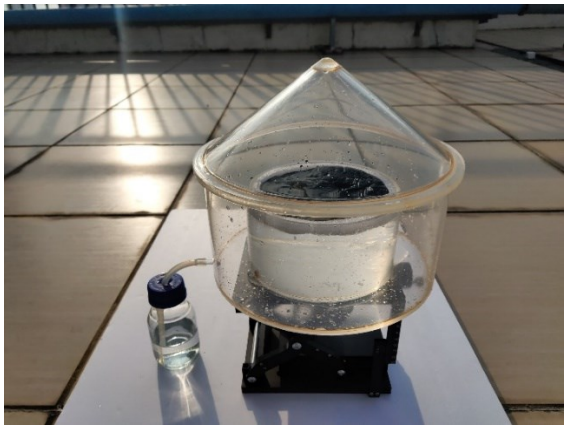

Figure S15. The optical picture of outdoor solar desalination setup.

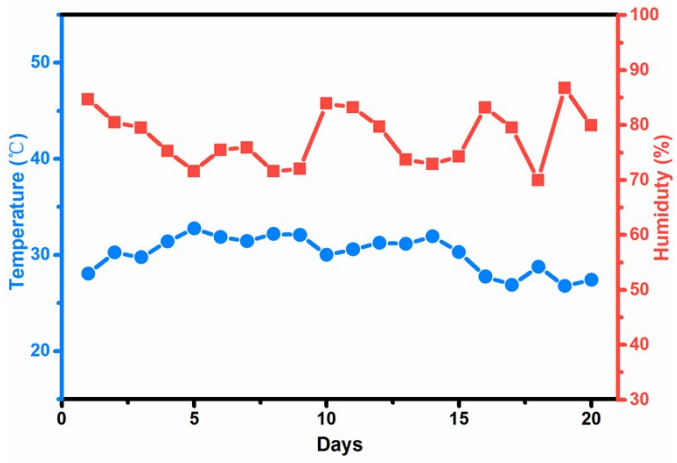

Figure S16. Ambient temperature and humidity data during outdoor test.

Note S5. Measurement of adsorption performance.

Methylene blue was taken as a representative organic dye to further study the adsorption performance of the samples in water treatment. The adsorption performance of pollen carbon cells and hydrogels has been studied separately. The Cu-PC with large specific surface area shows high adsorption performance. As shown in **Figure S17a**, the saturated adsorption capacity of Cu-PC is 508 mg g^{-1}, the process of Cu doping further increases the specific surface area of pollen carbon cells, so the saturated adsorption capacity of $Cu_{1.0}$-PC (532 mg g^{-1}) is slightly larger than that of Cu-PC. The D-PC obtained by direct carbonization without $CuCl_2$ activation shows extremely low saturated adsorption capacity of 2.3 mg/g (**Figure S17b)**. The adsorption performance of the hydrogels is shown in **Figure S17c**, the adsorption performance of pure PVA hydrogel is lower than 0.8 mg/g, when pollen carbon cells are added to the hydrogel, the adsorption performance of the $L_{2.5}$-$Cu_{1.0}$-PC hydrogel (2.9 mg/g) is greatly enhanced, which proves the superiority of dual adsorption of pollen carbon cells and hydrogel. The optical picture of the adsorption performance is shown in **Figure S18.**

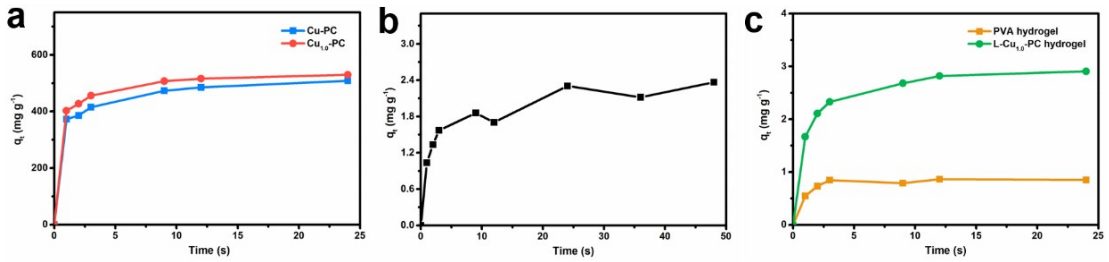

Figure S17. Adsorption kinetics fitting of (a) Cu-PC and $Cu_{1.0}$-PC, (b) D-PC (prepared by direct carbonize natural rape pollens without adding $CuCl_2$), and (c) PVA hydrogel and $L_{2.5}$-$Cu_{1.0}$-PC hydrogel.

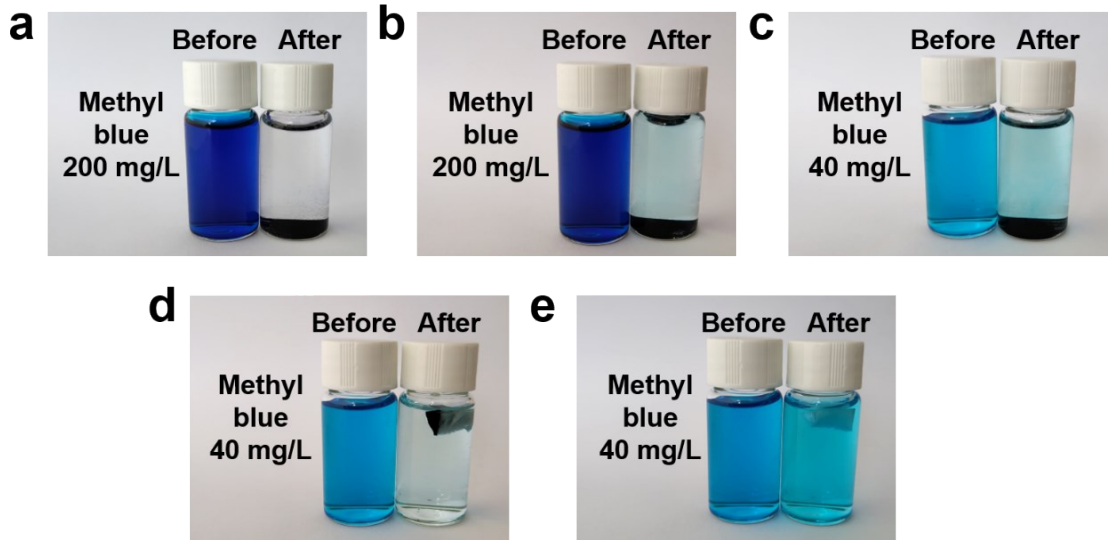

Figure S18. The capability of (a) $Cu_{1.0}$-PC, (b) Cu-PC, (c) D-PC (prepared by direct carbonize natural rape pollens without adding $CuCl_2$), (d) $L_{2.5}$-$Cu_{1.0}$-PC hydrogel, and (e) pure PVA hydrogel to remove water-soluble organic dyes.

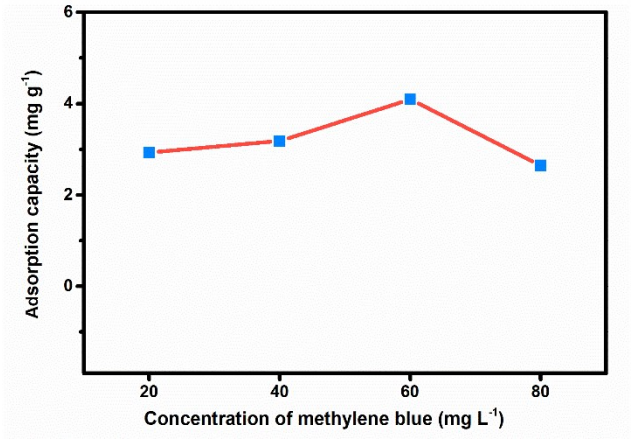

Figure S19. The saturated adsorption capacity of $L_{2.5}$-$Cu_{1.0}$-PC at different methylene blue concentrations.

Table S2. Solar steam generation performance comparison.

Sample	Evaporation rate ($kg\ m^{-2}h^{-1}$)	Conversion efficiency (%)	Reference
surface modified	1.37	85.3	[1]

coconut fiber (SCF)			
C-L-Wood	1.08	74.0%	2
porous carbon/polyaniline foam	1.496	87.3%	3
$BiVO_4$/graphene hydrogels	1.6	87%	4
pDA-rGO-PTFE	1.45	93,8%	5
fractal carbonized pomelo peels	1.95	92.4%	6
Drilled wood	1.04	75%	7
Surface-carbonized balsa wood	0.80	57%	8
PPy–wood	1.33	83%	9
Carbonized lotus seedpods	1.30	86.5%	10
ACF felt	1.22	79.4%	11
Carbonized tissue membrane	4.45(3sun)	95% (3sun)	12
Carbonized daikon	1.57	85.9%	13
Carbonized rice straw	1.2	75.8%	14
Three-dimensional carbon foams	1.26	80.1%	15
biomass aerogel	1.39	84, 68%	16
(PPy/Alg) hydrogel	1.15	54.12%	17
M-PPy sponge	1.447	84.72%	18

CG@MPT-h sponges	1.13	78.9%	[19]
K-wood	1.22	81.4%	[20]
polydopamine-filled cellulose aerogel	1.36	86%	[21]
Sandwich Photothermal Membrane	1.87	89%	[22]
$L_{2.5}$-$Cu_{1.0}$-PC hydrogel	2.08	85.6%	This work

References

1. J. Li, X. Zhou, G. Chen, F. Wang, J. Mao, Y. Long, H. Sun, Z. Zhu, W. Liang and A. Li, *Sol. Energy Mater. Sol. Cells*, 2021, **222**, 110941.
2. H. Liu, C. Chen, G. Chen, Y. Kuang, X. Zhao, J. Song, C. Jia, X. Xu, E. Hitz, H. Xie, S. Wang, F. Jiang, T. Li, Y. Li, A. Gong, R. Yang, S. Das and L. Hu, *Advanced Energy Materials*, 2018, **8**, 1701616.
3. K. Wang, Z. Cheng, P. Li, Y. Zheng, Z. Liu, L. Cui, J. Xu and J. Liu, *J. Colloid Interface Sci.*, 2021, **581**, 504-513.
4. L. Noureen, Z. Xie, M. Hussain, M. Li, Q. Lyu, K. Wang, L. Zhang and J. Zhu, *Sol. Energy Mater. Sol. Cells*, 2021, **222**, 110952.
5. B. L. Bai, X. H. Yang, R. Tian, X. X. Wang and H. B. Wang, *Desalination*, 2020, **491**, 10.
6. Y. Geng, W. Sun, P. Ying, Y. Zheng, J. Ding, K. Sun, L. Li and M. Li, *Adv. Funct. Mater.*, 2020, DOI: 10.1002/adfm.202007648, 2007648.
7. Y. Kuang, C. Chen, S. He, E. M. Hitz, Y. Wang, W. Gan, R. Mi and L. Hu, *Advanced materials* 2019, **31**, 1900498.
8. S. He, C. Chen, Y. Kuang, R. Mi, Y. Liu, Y. Pei, W. Kong, W. Gan, H. Xie, E. Hitz, C. Jia, X. Chen, A. Gong, J. Liao, J. Li, Z. J. Ren, B. Yang, S. Das and L.

Hu, *Energy & Environmental Science*, 2019, **12**, 1558-1567.

9. W. Huang, G. Hu, C. Tian, X. Wang, J. Tu, Y. Cao and K. Zhang, *Sustainable Energy & Fuels*, 2019, **3**, 3000-3008
10. J. Fang, J. Liu, J. J. Gu, Q. L. Liu, W. Zhang, H. L. Su and D. Zhang, *Chemistry of Materials*, 2018, **30**, 6217-6221.
11. H. R. Li, Y. R. He, Y. W. Hu and X. Z. Wang, *ACS Applied Materials & Interfaces*, 2018, **10**, 9362-9368.
12. Y. Chen, Y. Shi, H. Kou, D. Liu, Y. Huang, Z. Chen and B. Zhang, *ACS Sustainable Chemistry & Engineering*, 2019, **7**, 2911-2915.
13. M. M. Zhu, J. L. Yu, C. L. Ma, C. Y. Zhang, D. X. Wu and H. T. Zhu, *Sol. Energy Mater. Sol. Cells*, 2019, **191**, 83-90.
14. Q. L. Fang, T. T. Li, Z. M. Chen, H. B. Lin, P. Wang and F. Liu, *ACS Applied Materials & Interfaces*, 2019, **11**, 10672-10679.
15. P. Qiu, F. Liu, C. Xu, H. Chen, F. Jiang, Y. Li and Z. Guo, *Journal of Materials Chemistry A*, 2019, **7**, 13036-13042
16. J. Li, X. Zhou, Y. Jing, H. Sun, Z. Zhu, W. Liang and A. Li, *ACS applied materials & interfaces*, 2021, **13**, 12181-12190.
17. S. H. Park, J. H. Park, J. Kim and S. J. Lee, *Desalination*, 2021, **500**, 114900.
18. Y. Fan, W. Bai, P. Mu, Y. Su, Z. Zhu, H. Sun, W. Liang and A. Li, *Sol. Energy Mater. Sol. Cells*, 2020, **206**, 110347.
19. X. Wang, Z. Li, Y. Wu, H. Guo, X. Zhang, Y. Yang, H. Mu and J. Duan, *ACS Applied Materials & Interfaces*, 2021, **13**, 10902-10915.
20. D. Li, D. Han, C. Guo and C. Huang, *ACS Applied Energy Materials*, 2021, **4**, 1752-1762.
21. Y. Zou, J. Zhao, J. Zhu, X. Guo, P. Chen, G. Duan, X. Liu and Y. Li, *ACS Applied Materials & Interfaces*, 2021, **13**, 7617-7624.
22. C. Tian, J. Liu, R. Ruan, X. Tian, X. Lai, L. Xing, Y. Su, W. Huang, Y. Cao and J. Tu, *Small*, 2020, **16**, 2000573.